Supporting Information

Highly stable Fe-based catalyst from partially leached Al-Fe-Si alloy for hydrogenation CO_2 to light olefins

Haipeng Chen,*[a] Wenran Meng,[ac] Yiming Li,[a] Shuwen Hou,[a] Weiwei Yuan,[a] Wenqiang Li,[a] Minjian Yang*[b] and Xun Feng*[a]

[a] College of Chemistry and Chemical Engineering, Henan Key Laboratory of Function-Oriented Porous Materials, Luoyang Normal University, Luoyang 471934, China

[b] College of Chemical Engineering, Guizhou University of Engineering Science, Bijie 551700, China

[c] College of Chemistry and Chemical Engineering, Henan Polytechnic University, Jiaozuo 454000, China

*Corresponding authors:

chenhaipeng@lynu.edu.cn (H.P. Chen)

honglinymj@163.com (M.J. Yang)

fengx@lynu.edu.cn (X. Feng)

No of Pages: 20

Summary:

Experimental Section

Table S2. Catalytic performances of CO_2 hydrogenation over the the Fe-based catalysts from leaching with different KOH concentration.

Table S3. Summary of Fe-based catalysts for CO_2 hydrogenation to $C_2^=$-$C_4^=$ species.

Table S4. Catalytic performances of CO_2 hydrogenation over the Fe-based catalysts at different temperatures.

References

Experimental Section

Preparation of the Fe-based catalyst

The alkali leaching method was applied for the preparation of Fe-based catalyst. Typically, 1.0 g of Al-Fe-Si alloy (Hengshi Metal Alloy Powder Co., LTD, China) was added into a flask with KOH solution (Macklin, China). The mixture was then heated to 85 °C and stirred for 3.0 h to dissolve the Si and Al of the Al-Fe-Si alloy. The obtained product was centrifuged and washed ten times with deionized water and ethanol, respectively. Potassium (5.0 wt%) was added into the Fe-based catalyst as the promoter via wet impregnation method using K_2CO_3 solution (Macklin, China). All the samples were dried in a vacuum oven at at 60 °C for 12.0 h. Using KOH as the leaching agent not only enables the efficient and controllable dissolution of Al and Si from the Al-Fe-Si alloy due to its high alkalinity, forming a residual alloy framework, but also ensures that only K^+ is introduced into the catalytic system, avoiding the interference of multiple alkali metal cations on catalytic performance.

CO_2 hydrogenation

For CO_2 hydrogenation, a stainless-steel tube with 8.0 mm inner diameter was served as the fixed-bed reactor. To eliminate temperature and concentration gradient, 0.5 g catalyst was first blended with 1.0 mL inert quartz sand (particle size: 40 - 80 mesh), and then the mixture was placed into the reactor. The catalyst was reduced at 350 °C for 5.0 h under a H_2/N_2 gas mixture containing 80% H_2. After cooled down to room temperature, a H_2/CO_2 mixture ($H_2/CO_2 = 3$) balanced with N_2 were introduced into the reactor as feed gas. The reactor was gradually pressurized to 2.0 MPa using a back-pressure valve, and then heated to the reaction temperature. After a time-on-stream (TOS) of at least 2.0 h, all hydrogenation products were analyzed using an online GC system.

Characterization

X-ray diffraction (XRD) was carried out on a Rigaku D/Max-rB X-ray diffractometer in a step size of 0.02º operated at 40 kV and 40 mA with Cu Kα irradiation (λ = 1.54178 Å). Scanning electron microscopy (SEM) was performed on a ZEISS Sigma 300 electron microscope operating at 5.0 kV. Spherical aberration-corrected scanning transmission electron microscopy (AC-STEM) and the corresponding energy-dispersive X-ray spectroscopy (EDX) mapping were performed on a JEOL ARM200F microscope with an acceleration voltage of 200 kV. Raman spectroscopy was carried out on an inVia Raman microscope with a semiconductor laser as the excitation source (532 nm, 0.1 mW). X-ray photoelectron spectroscopy (XPS) was carried out on a Thermo Escalab 250Xi spectrometer in an energy step size of 1.0 eV with a monochromatic Al Kα X-ray source (hv = 1486.6 eV). *In-situ* diffuse reflectance infrared Fourier transform spectroscopy (*in-situ* DRIFT) was carried out on a Thermo IS 50 spectrometer equipped with an MCT detector. Temperature-programmed desorption (CO_2-TPD) was carried out on an AutoChem II 2720 chemisorption analyzer.

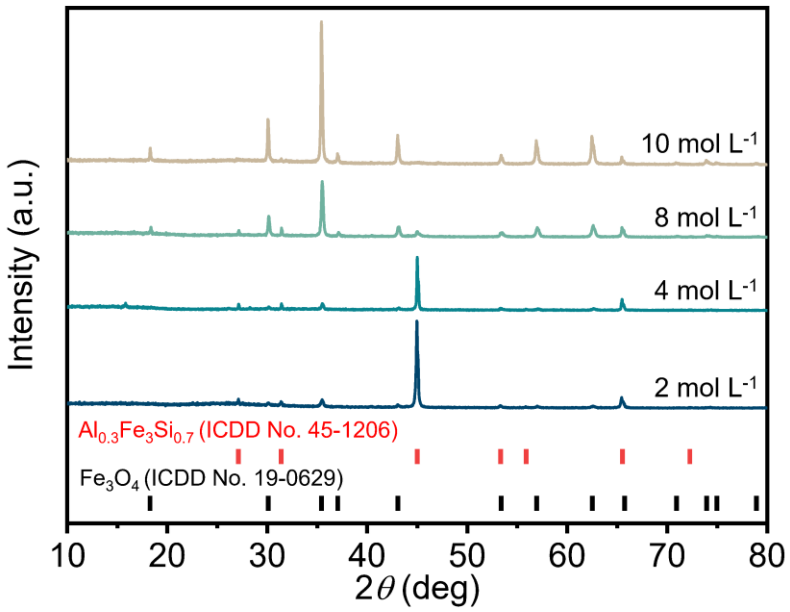

Figure S1. XRD patterns of the Fe-based catalysts from leaching with 2, 4, 8 and 10 mol L^{-1} KOH.

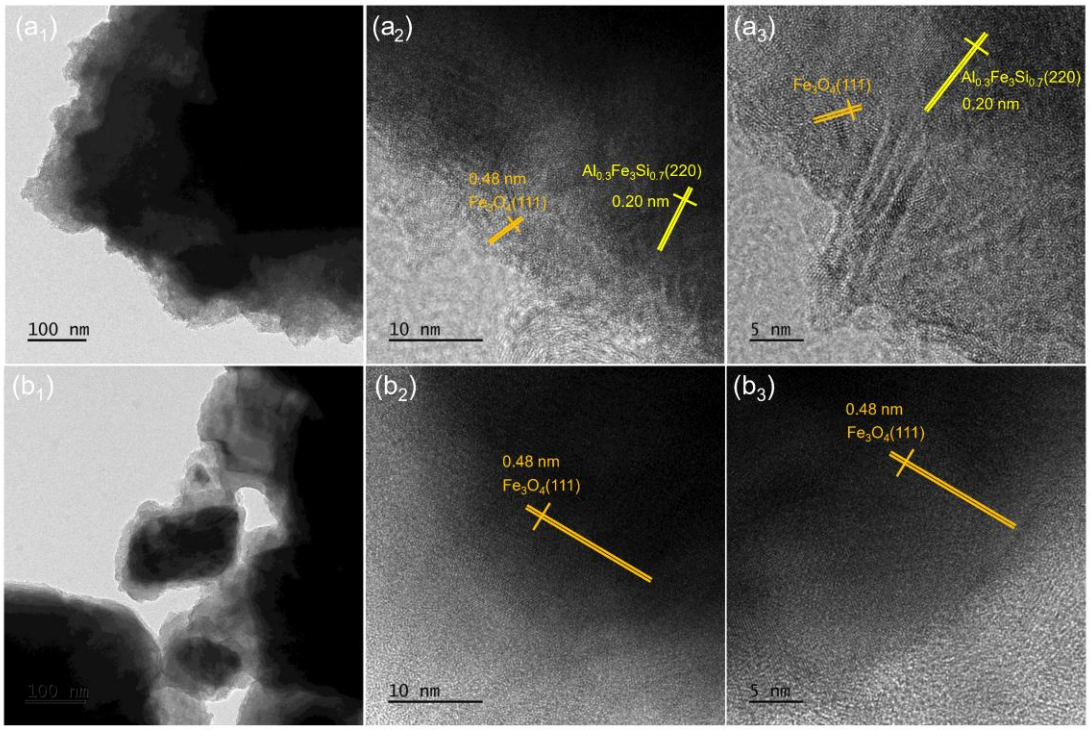

Figure S2. HRTEM images of the Fe-based catalysts from leaching with (a_1-a_3) 8 mol L^{-1} and (b_1-b_3) 10 mol L^{-1} KOH.

From the characterization results, it can be inferred that the KOH leaching process essentially alters the chemical composition and phase structure of the $Al_{0.3}Fe_3Si_{0.7}$ alloy through selective dissolution. When KOH solution contacts with Al-Fe-Si alloy, it will preferentially react with Al and Si in it and dissolve them. When the concentration of KOH is relatively low (such as 2 mol L^{-1}), the dissolution effect is limited, and the main structure of the alloy ($Al_{0.3}Fe_3Si_{0.7}$) is largely retained, while a small amount of Fe is oxidized to form Fe_3O_4 crystals. As the concentration of KOH increases (to 8 mol L^{-1}), more Al and Si are dissolved, forming a multiphase mixed structure in which Fe_3O_4 is embedded or coexists with the residual alloy phase. When the concentration of KOH is too high (10 mol L^{-1}), Al and Si are completely dissolved, the alloy phase completely disappears, and eventually a single Fe_3O_4 crystal structure is obtained. Therefore, from a structural perspective, the concentration of KOH controls the structural evolution process from "alloy phase dominant" to "alloy phase mixed with Fe_3O_4" and then to "pure Fe_3O_4 phase".

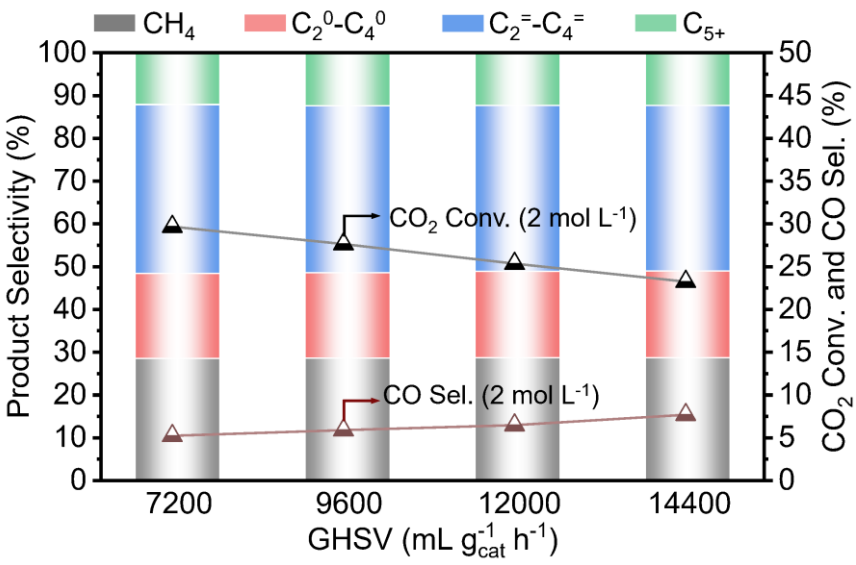

Figure S3. Product selectivity, CO_2 conversion, and CO selectivity of the Fe-based catalysts (2 mol L^{-1} KOH) under different GHSV conditions.

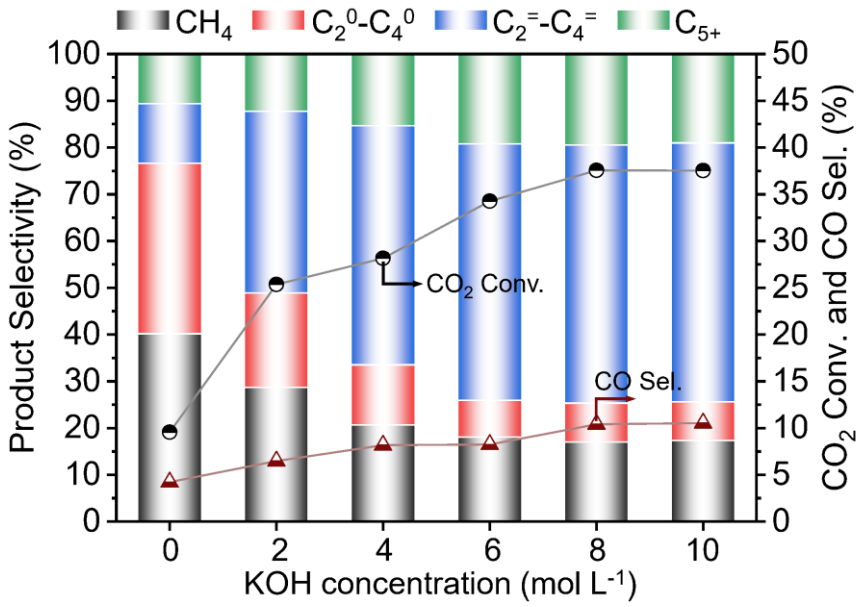

Figure S4. Product selectivity, CO_2 conversion and CO selectivity of the Fe-based catalysts from leaching with different KOH concentration. Conditions: T = 320 °C, P = 2.0 MPa, H_2/CO_2 = 3, TOS = 2 h, and GHSV = 12000 mL g_{cat}^{-1} h^{-1}.

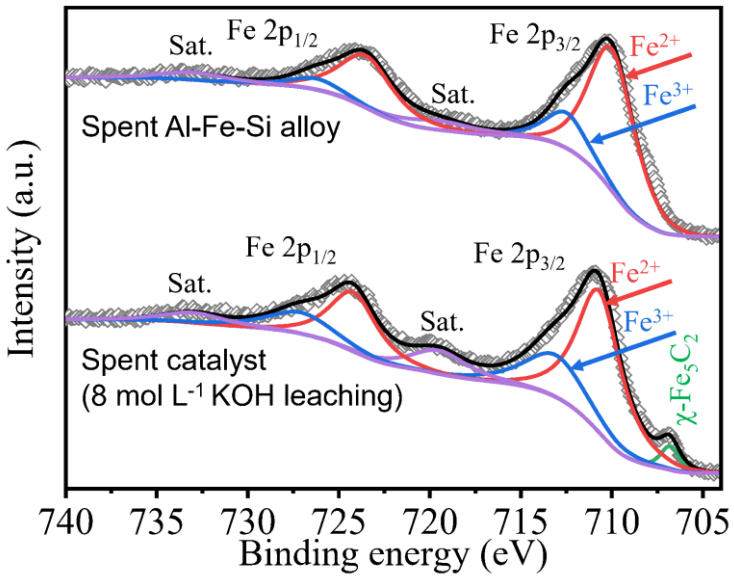

Figure S5. XPS spectra of the spent Al-Fe-Si alloy and spent Fe-based catalyst. Conditions: T = 320 °C, P = 2.0 MPa, H_2/CO_2 = 3, TOS = 2 h, and GHSV = 12000 mL g_{cat}^{-1} h^{-1}.

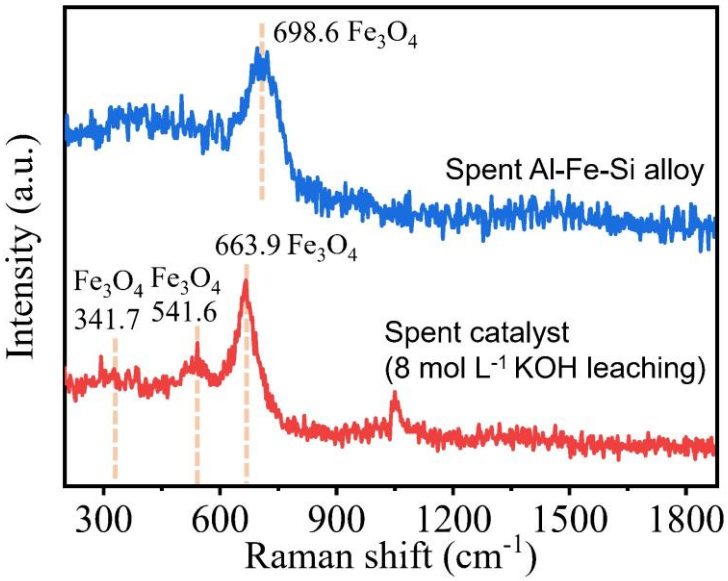

Fig. S6. Raman spectra of of the spent Al-Fe-Si alloy and spent Fe-based catalyst. Conditions: T = 320 °C, P = 2.0 MPa, H_2/CO_2 = 3, TOS = 2 h, and GHSV = 12000 mL g_{cat}^{-1} h^{-1}.

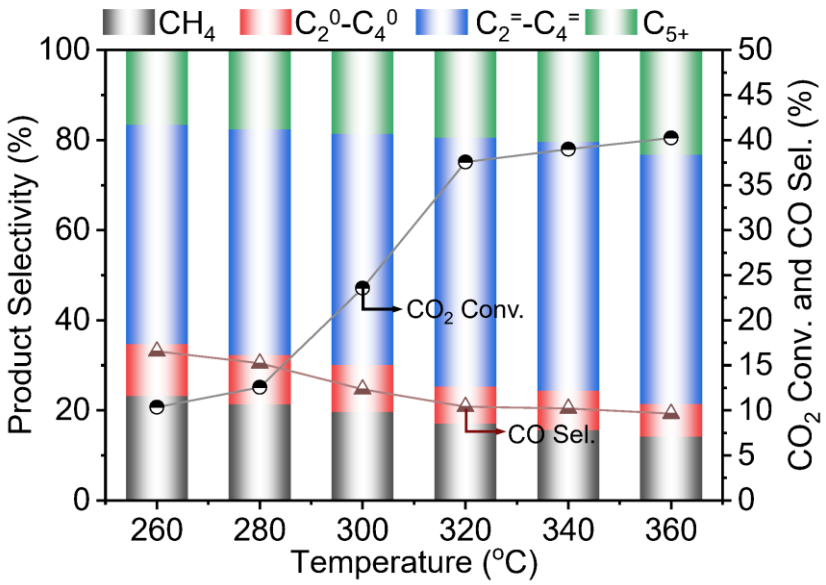

Figure S7. Product selectivity, CO_2 conversion and CO selectivity of the Fe-based catalyst (8 mol L^{-1} KOH leaching) under different reaction temperatures. Conditions: *P* = 2.0 MPa, H_2/CO_2 = 3, TOS = 2 h, and GHSV = 12000 mL g_{cat}^{-1} h^{-1}.

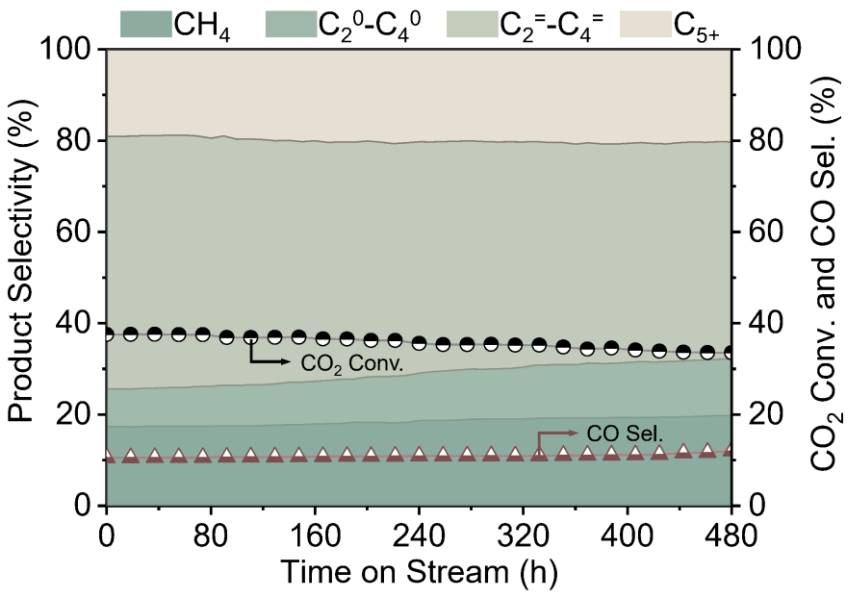

Figure S8. Catalytic stability of the Fe-based catalyst from leaching with 10 mol L^{-1} KOH. Conditions: T = 320 °C, P = 2.0 MPa, H_2/CO_2 = 3, and GHSV = 12000 mL g_{cat}^{-1} h^{-1}.

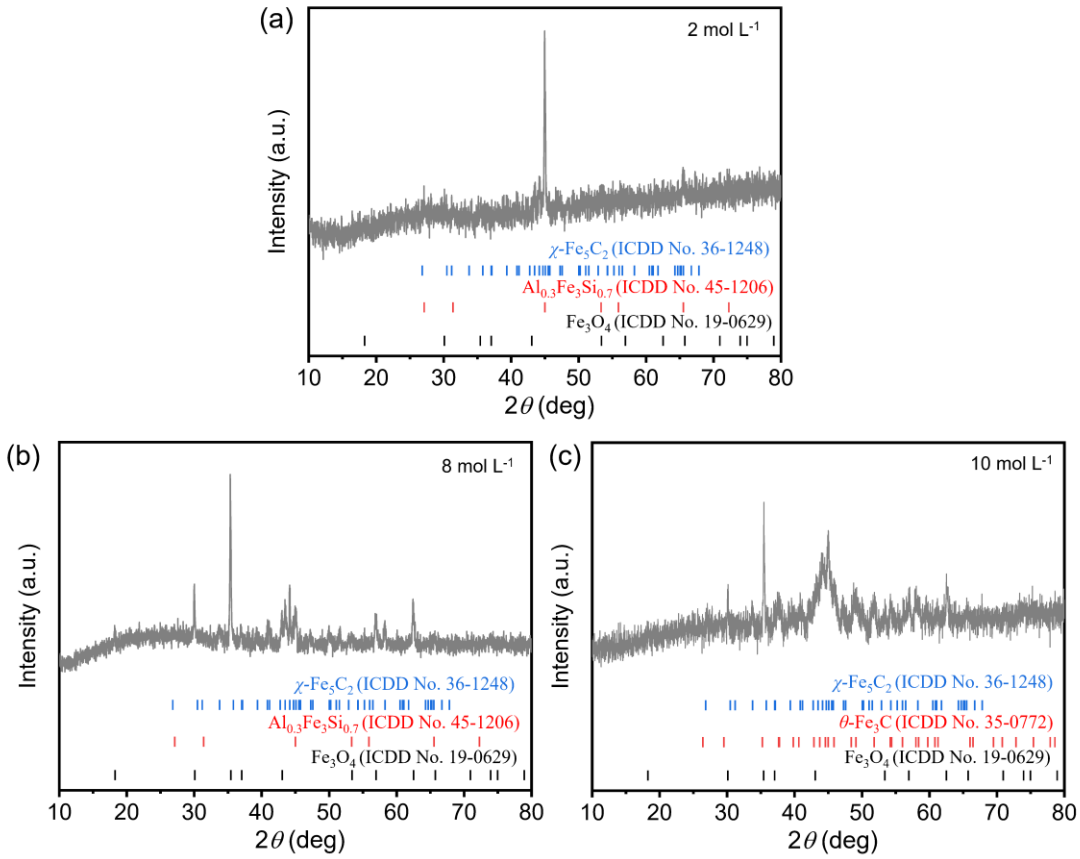

Figure S9. XRD patterns of the spent Fe-based catalysts from leaching with (a) 2 mol L^{-1}, (b) 8 mol L^{-1} and (c) 10 mol L^{-1} KOH. Conditions: T = 320 °C, P = 2.0 MPa, H_2/CO_2 = 3, TOS = 480 h, and GHSV = 12000 mL g_{cat}^{-1} h^{-1}.

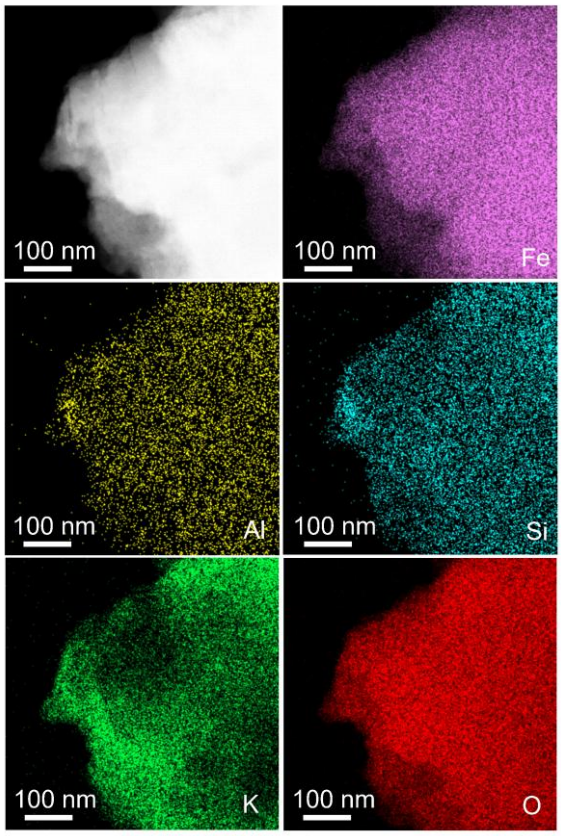

Figure S10. HAADF-STEM image and the corresponding EDX elemental mapping of the spent Fe-based catalysts from leaching with 2 mol L^{-1} KOH. Conditions: T = 320 °C, P = 2.0 MPa, H_2/CO_2 = 3, TOS = 480 h, and GHSV = 12000 mL g_{cat}^{-1} h^{-1}.

Table S1. Catalytic performances of the Fe-based catalysts under different GHSV conditions.

KOH concentration (mol L^{-1})	GHSV (mL g_{cat}^{-1} h^{-1})	CO_2 Conversion (%)	CO Selectivity (%)	Hydrocarbon distribution (%)				STY of $C_2^{=}$-$C_4^{=}$ (mg g_{cat}^{-1} h^{-1})
				CH_4	C_2^0-C_4^0	$C_2^{=}$-$C_4^{=}$	C_{5+}	
2	7200	29.7	5.2	28.5	19.9	39.5	12.1	125.1
	9600	27.6	5.9	28.6	19.9	39.1	12.4	152.4
	12000	25.4	6.5	28.7	20.2	38.8	12.3	172.7
	14400	23.2	7.7	28.7	20.3	38.6	12.4	186.6
8	7200	40.3	8.1	16.9	8.2	55.2	19.7	230.4
	9600	38.5	9.5	17.0	8.2	55.3	19.5	290.1
	12000	37.6	10.4	17.0	8.3	55.2	19.5	348.4
	14400	35.2	11.4	17.1	8.2	55.2	19.5	387.9

Table S2. Catalytic performances of CO_2 hydrogenation over the the Fe-based catalysts from leaching with different KOH concentration.

KOH concentration (mol L^{-1})	CO_2 Conversion (%)	CO Selectivity (%)	Hydrocarbon distribution (%)				STY of $C_2^{=}$-$C_4^{=}$ (mg g_{cat}^{-1} h^{-1})
			CH_4	C_2^0-C_4^0	$C_2^{=}$-$C_4^{=}$	C_{5+}	
0	9.6	4.2	40.2	36.5	12.7	10.6	21.8
2	25.4	6.5	28.7	20.2	38.8	12.3	172.7
4	28.2	8.2	20.6	12.9	51.2	15.3	247.9
6	34.3	8.3	18.1	7.8	54.8	19.3	323.1
8	37.6	10.4	17.0	8.3	55.2	19.5	348.4
10	37.5	10.5	17.4	8.2	55.4	19.0	348.7

Table S3. Summary of Fe-based catalysts for CO_2 hydrogenation to $C_2^=$-$C_4^=$ species.

Catalyst	H_2/CO_2 ratio	Temperature (^oC)	Pressure (MPa)	Space velocity	CO_2 conversion (%)	$C_2^=$-$C_4^=$ selectivity (%)	CO selectivity (%)	Ref.
Fe_2O_3@KO_2/MOR	3:1	375	3.0	5000 mL g^{-1} h^{-1}	48.3	33.3	N/A	[1]
Fe_5C_2-10K/Al_2O_3	3:1	320	3.0	3600 mL g^{-1} h^{-1}	31.5	35.8	18.6	[2]
K-Fe-Ti LMO	3:1	320	2	1000 h^{-1}	36.3	60.0	65	[3]
K-Fe	3:1	340	2	N/A	38.0	34.0	7.3	[4]
Fe-K/HPCMs-1	3:1	400	3.0	3600 mL g^{-1} h^{-1}	33.4	18.0	38.9	[5]
Fe_2O_3-CT600	3:1	300	1.0	1140 mL g^{-1} h^{-1}	23.0	46.1	N/A	[6]
Fe-Cr-K/Nb_2O_5	3:1	400	0.1	3600 mL g^{-1} h^{-1}	20.0	25.0	33	[7]
Fe_3O_4	3:1	340	1.0	4800 mL g^{-1} h^{-1}	27.0	5.7	35.9	[8]
Fe/K/C	3:1	350	3	24000 mL g^{-1} h^{-1}	38.5	38.8	17	[9]
10Mn-Fe_3O_4	3:1	350	2.0	4000 mL g^{-1} h^{-1}	44.7	46.2	9.4	[10]
K/Fe@NC	3:1	320	3	7200 mL g^{-1} h^{-1}	30.6	33.1	18.6	[11]
Fe-based catalyst	3:1	320	2	12000 mL g^{-1} h^{-1}	37.6	55.2	10.4	This work

Table S4. Catalytic performances of CO_2 hydrogenation over the Fe-based catalysts at different temperatures.

Temperature	CO_2 Conversion	CO Selectivity	Hydrocarbon distribution (%)				STY of $C_2^=$-$C_4^=$ (mg g_{cat}^{-1} h^{-1})
	(%)	(%)	CH_4	C_2^0-C_4^0	$C_2^=$-$C_4^=$	C_{5+}	
260	10.3	16.6	23.3	11.5	48.7	16.5	103.7
280	12.6	15.2	21.4	10.9	50.1	17.6	130.3
300	23.6	12.4	19.7	10.4	51.2	18.7	245.3
320	37.6	10.4	17.0	8.3	55.2	19.5	348.4
340	38.9	10.2	15.7	8.7	55.3	20.3	361.2
360	40.2	9.7	14.2	7.2	55.3	23.3	373.0

References

1 A. Ramirez, A.D. Dutta Chowdhury, A. Dokania, P. Cnudde, M. Caglayan, I. Yarulina, E. Abou-Hamad, L. Gevers, S. Ould-Chikh, K. De Wispelaere, V. van Speybroeck and J. Gascon, *ACS Catal.*, 2019, **9**, 6320–6334.

2 I.A. da Silva and C.J.A. Mota, *Front. Energy Res.*, 2019, **7**, 49.

3 X. Wang, D. Wu, J. Zhang, X. Gao, Q. Ma, S. Fan and T. Zhao, *Appl. Catal. A*, 2019, **573**, 32–40.

4 Z. You, W. Deng, Q. Zhang and Y. Wang, *Chin. J. Catal.*, 2013, **34**, 956–963.

5 C. Dai, A. Zhang, M. Liu, J. Li, F. Song, C. Song and X. Guo, *RSC Adv.*, 2016, **6**, 10831–10836.

6 M. Albrecht, U. Rodemerck, M. Schneider, M. Bröring, D. Baabe and E. V. Kondratenko, *Appl. Catal. B*, 2017, **204**, 119–126.

7 J. Liu, A. Zhang, X. Jiang, M. Liu, J. Zhu, C. Song and X. Guo, *Ind. Eng. Chem. Res.*, 2018, **57**, 9120–9126.

8 Y. Xu, C. Shi, B. Liu, T. Wang, J. Zheng, W. Li, D. Liu and X. Liu, *Catal. Sci. Technol.*, 2019, **9**, 593–610.

9 A. Ramirez, L. Gevers, A. Bavykina, S. OuldChikh, J. Gascon, *ACS Catal.*, 2018, **8**, 9174–9182.

10 J. Jiang, C. Wen, Z. Tian, Y. Wang, Y. Zhai, L. Chen, Y. Li, Q. Liu, C. Wang and L. Ma, *Ind. Eng. Chem. Res.*, 2020, **59**, 2155–2162.

11 J. Liu, A. Zhang, X. Jiang, G. Zhang, Y. Sun, M. Liu, F. Ding, C. Song and X. Guo, *Ind. Eng. Chem. Res.*, 2019, **58**, 4017–4023.